Contents lists available at ScienceDirect

Arabian Journal of Chemistry

journal homepage: www.ksu.edu.sa

Controlling cisplatin release by synergistic action of silver-cisplatin on monodispersed spherical silica for targeted anticancer and antibacterial activities

Suriya Rehman [a], Vijaya Ravinayagam [b,*], Suhailah S. Al-Jameel [c], Syed Mehmood Ali [d], Sukainah Z. Alzayer [e,f], Zahrah M. Alfaraj [e,f], Atheer Alboeid [e,f], Nawal Alamri [e,f], Sakinah H Al Isam [e,f], H. Dafallae [g], Sugapriya Dhanasekaran [h], Gazali Tanimu [i], Firdos Alam Khan [j], B. Rabindran Jermy [k,*]

[a] Department of Epidemic Diseases Research, Institute for Research & Medical Consultations (IRMC), Imam Abdulrahman Bin Faisal University, Dammam 31441, Saudi Arabia
[b] Deanship of Scientific Research & Department of NanoMedicine Research, Institute for Research & Medical Consultations, Imam Abdulrahman Bin Faisal University, 31441 Dammam, Saudi Arabia
[c] Department of Chemistry, College of Science, Imam Abdulrahman Bin Faisal University, 31441 Dammam, Saudi Arabia
[d] Department of Biomedical Engineering, College of Engineering, Imam Abdulrahman Bin Faisal University, 31441 Dammam, Saudi Arabia
[e] IRMC-InP-2021 Program, Department of Epidemic Diseases Research & Department of Nano-Medicine Research, Institute for Research and Medical Consultations (IRMC), Imam Abdulrahman Bin Faisal University, 31441 Dammam, Saudi Arabia
[f] College of Dentistry, Imam Abdulrahman Bin Faisal University, 31441 Dammam, Saudi Arabia
[g] College of Engineering Research (CER), King Fahd University of Petroleum and Minerals, 31261 Dhahran, Saudi Arabia
[h] Department of Medical Lab Sciences, College of Applied Medical Sciences, Prince Sattam Bin Abdulaziz University, Wadi Ad Dawasir Campus, Saudi Arabia
[i] Center for Refining and Advanced Chemicals, Research Institute, King Fahd University of Petroleum and Minerals, P.O. Box 5040, Dhahran 31261, Saudi Arabia
[j] Department of Stem Cell Research, Institute for Research and Medical Consultations (IRMC), Imam Abdulrahman Bin Faisal University, 31441 Dammam, Saudi Arabia
[k] Department of NanoMedicine Research, Institute for Research & Medical Consultations, Imam Abdulrahman Bin Faisal University, 31441 Dammam, Saudi Arabia

ARTICLE INFO

Keywords:
Antibacterial
Anticancer
Drug Delivery
Monodispersed silica
Silver nanoparticles

ABSTRACT

Recently, metal-based nanoformulations have been explored for targeted cancer therapeutics. In this study, synergistic therapeutic action of silver (Ag)-cisplatin nanoparticles loaded on monodispersed spherical silica (MSS) was investigated to evaluate anti-cancer (HCT-116 and HeLa cells) and antibacterial activity (*P.aeruginosa*, and *S.aureus*). Four different wt% of Ag (1, 2, 4 and 6 wt%) was loaded on MSS using a wet impregnation method. Characterization using XRD revealed the cubic phase of Ag nanoparticles with (111), (200) and (220) plane on MSS. The chemical state, dispersion of Ag and synergistic cohabitation with cisplatin (Cpt) was identified using diffuse reflectance UV–visible spectroscopy (DR-UV Vis), X-ray photoelectron spectroscopy (XPS), Scanning electron microscopy/energy-dispersive X-ray spectrometry (SEM-EDS) and High-resolution transmission electron microscopy (HR-TEM). Zeta potential analysis indicated an increase in hydrodynamic diameter with high colloidal stability (–23.3 to −28.5 mV). The percentage cumulative Cpt release was studied using automated Franz cell and dialysis membrane technique. The effect of Cpt release on 4 wt%Ag impregnated on different shaped supports was investigated using cubic SBA-16 (Santa Barbara Amorphous), MFI type Ti-ZSM-5 (Zeolite Socony Mobil #5), hexagonal mesosilicalite, nanotube halloysite, and Ag-silicalite, respectively. Drug release study indicates that Ag loading controls the Cpt release. The kinetics of drug release for the different formulations was examined using Korsmeyers-Peppas model. Release constant (k) and release exponent (n) were utilized for the rate of drug release and diffusion mechanisms, respectively. The *in vitro* study revealed an efficient interaction of nanoformulations promoting both antibacterial and anticancer activities.

* Corresponding authors.
E-mail addresses: vrnayagam@iau.edu.sa (V. Ravinayagam), rjermy@iau.edu.sa (B. Rabindran Jermy).

https://doi.org/10.1016/j.arabjc.2024.105661
Received 27 June 2023; Accepted 28 January 2024
Available online 9 February 2024

1. Introduction

Nanobiotechnology research has been rising steadily to develop uniformly sized nanoparticles for targeted nanotherapy. The nanoparticle shape, particle size, and textural characteristics such as surface area and pore size distributions of silica-based nanocarrier influence the drug solubility, drug release efficacy, and bioavailability (Spitzmüller et al., 2023). The porous silica nanocarrier with particle sizes ranging between 10 and 100 nm has been reported to increase the circulation time and avoid macrophage detection during the circulation. On the other hand, particle sizes less than 10 nm or larger than 100 nm are either rapidly cleared or difficult for renal clearance (Chandrakala et al., 2022). Nano design of monodispersed silica with tailor-made tight particle sizes has recently been explored for biomedical applications (Niculescu., 2020, Jermy et al., 2020). Recently, metal-based formulations have been explored for coating medical implants, diagnostic and cancer therapeutics (Kumar et al., 2023). Silver nanoparticles (AgNPs) are known to exhibit antimicrobial activity in the oxidized state, whereas soluble silver salts have been previously used for their bactericidal property (Urnukhsaikhan et al., 2021). AgNPs have been prospected to be used in targeted cancer therapeutics using nanotechnology (Kovács et al., 2022). Nanocarrier design based on Ag/silica nanocomposite has been shown to provide multifunctional capabilities against microbes, cancer cells, and inflammatory diseases (Rehman et al., 2020b, Aldossary et al., 2022, Hemlata et al., 2020). Different mechanisms of action have been suggested to figure out the effectiveness of silver ions, such as the high affinity of monovalent silver ions to sulfhydryl (S-H) groups of proteins, the interaction of Ag^{+} with DNA replication inactivates vital enzymes and affect the replication ability of bacterial DNA, leading to cell death (Mohanbaba et al., 2016, Helmiyati et al., 2019).

In the present studies, dual metal/metal oxide nanoparticles exhibiting a synergistic action compared to mono metal have been explored for anticancer and antibacterial activity (Abdulrehman et al., 2020, Dubey et al., 2022, Subhan et al., 2022). Molybdenum nanosheet/Ag nanocomposite with chitosan (CS/MoS_2/Ag) exhibited an antibacterial (*E. coli* and *S aureus*) and anticancer activity. The presence of charged nanoparticles (Mo^{4+} and Ag^{+}) tends to generate reactive oxygen species, exhibit oxidative stress, and induce cancer cell death (MCF-7) (Kasinathan et al., 2021). Ag/Cu doped with boron was reported to be an effective nanoformulation against osteoblast infection (Abdulrehman et al., 2020). Recently, Ag/spiky silica nanocomposite has been reported for dual delivery of nanosilver and vancomycin for high antibacterial activity (Ni et al., 2022). Yolk-shell based Ag/silica using chemo/starvation/metal ion multimodality concept has shown to be an effective strategy to interrupt the energy supply and kill cancer cells (Zhang et al., 2020). Ag and Zn oxide nanoparticles prepared through the green synthesis technique exhibited a synergistic effect with antifungal and anticancer activities (Hashem et al., 2023). Dual metal doping of Ag and Ce on zinc oxide nanoparticles was reported to influence the homogeneous distribution of metals and cytotoxic effect against breast cancer cells (Al-Enazi et al., 2023]. The combination of Au-Ag nanoparticles was found to be less toxic against human cells and more effective against drug-resistance bacteria (Singh et al., 2022). Bimetallic ZnO-Ag nanoparticles (particle sizes 30–130 nm) synthesized using the laser ablation method are more effective against Hela and HCT-116 cells than mono metals (Elsayed et al., 2022).

In earlier studies, synergistic effects of Ag-Pt nanoparticles have been reported against antimicrobial and anti-cancer activities (Yang et al., 2020, Gao et al., 2021). The platinum-based drug, such as Cpt (*cis*-diamminedichloroplatinum (II)) have been used for treating a wide range of cancers. However, the drug also imparts several side effects, such as nephrotoxicity, drug resistance, nerve dysfunction, repeated dose toxicity, and hearing impairment (Gilani et al., 2022). To the best of our knowledge, the effects of Ag and Cpt over monodispersed spherical silica for targeted therapeutics have not been studied. Developing such a nanocomposite is not straightforward as impregnation with metal/metal oxides tends to change the textural uniformity of nanocarriers (Chang et al., 2022, Yan et al., 2021). Therefore, we have examined the synergistic effect of Ag and Cpt on MSS by using different weight percentage Ag loadings (1–6 wt%) and studied the effect against bacterial and cancer cells. For comparative study, an intermediate loading of 4 wt% Ag was loaded on different structured nanocarriers such as cubic SBA-16, MFI type Ti-ZSM-5, hexagonal mesosilicalite, nanotube halloysite, and Ag-silicalite. The samples were further characterized using various physico-chemical analyses. *In vitro* Cpt release was studied using Franz cells/dialysis membrane and further studied for antibacterial and anticancer activity.

2. Materials and methods

Silver nitrate (ACS reagent grade, ≥99 %), tetraethyl orthosilicate (TEOS, reagent grade, 98 %), Pluronic F127, cisplatin (crystalline), titanium (IV) isopropoxide (TTIP, 97 %), tetrapropyl ammonium bromide (TPABr, 98 %), Ludox AS-40 colloidal silica (40 wt% suspension in H_2O), Tetrabutylammonium hydroxide solution (TPAOH, ~40 % in water), Sodium fluoride (NaF, ≥99 %, ACS reagent), Aluminum nitrate nonahydrate ($Al(NO_3)_3{\cdot}9H_2O$, ≥98 %), Hexadecyltrimethylammonium bromide (CTAB, ≥98 %), sodium hydroxide (NaOH, reagent grade, ≥98 %) and halloysite with diameter of 30–70 nm × 1–3 μm length were purchased from Sigma Aldrich, Chemie Holding GmbH, Taufkirchen, Germany. MSS (particle effective diameter size ~ 80.9 nm) is a 99 % pure monodispersed spherical silica (SUPSIL STANDARD) with silanol functional groups was purchased from Superior Silica LLC, 341 E Alamo Drive, Chandler, AZ, 85225, USA (https://superiorsilica.com/products/). Structured silica like SBA-16 was prepared using the sol–gel technique. Pluronic F127 was used as a template, while TEOS was used as a silica source (Balasamy et al., 2019). TiZSM-5 was obtained using TTIP, and TPABr template using hydrothermal technique. In brief, 11.42 g of Ludox AS-40 was taken and mixed with 8 g of TPAOH for 1 h. Then 0.31 g of NaF (F/Si ratio 1), 0.63 mL of TTIP and 0.96 g of $Al(NO_3)_3{\cdot}9H_2O$ was added and stirred (300 rpm) for 30–60 min. Then 0.93 g of NaOH dissolved in 9 mL water was added dropwise and stirred overnight. The solution was then transferred in a 250 mL autoclave bomb and kept in a static oven hydrothermally treated at 160 °C for 72 h. Final sample was recovered by filtration, drying, and calcination (550 °C for 6 h). Silicalite was synthesized using TPABr as a template and Ludox AS-40 as silica source. Silicalite was then changed to mesosilicalite in the presence of CTAB template using a top-down approach (Aldossary et al., 2022).

2.1. Preparation of 1–6 wt% Ag/MSS (Antibacterial Study)

For 1 wt% Ag loading, 0.016 g of silver nitrate was dissolved in 30 mL distilled water for 30 min. Then 1.0 g of predried MSS was added, and the solution mixture was allowed to stir (300 rpm) for 12 h. The mixture was then heated at 120 °C for 6 h. The obtained sample was powdered using mortar and pestle and finally calcined in air at 500 ℃ for 3 h (5 °C/min). Likewise, 2 wt% (0.031 g), 4 wt% (0.063 g) and 6 wt % (0.094 g) of Ag was loaded over MSS (1 g) and then calcined in air at 500 ℃ for 3 h (5 °C/min).

Following a similar procedure, 4 wt% Ag (0.063 g) was loaded per gram of different supports such as SBA-16 (Santa Barbara Amorphous), TiZSM-5 (Zeolite Socony Mobil #5), mesosilicalite, halloysite, and Ag-silicalite, respectively. A detailed list of final samples was presented in Table 1.

2.2. 1–6 wt% Ag/MSS or structured Silica/Cpt (Anticancer Study)

In the first step, cisplatin (~30 mg) was mixed in 10 mL of normal saline solution (10 mL) at 40 °C and then stirred (200 rpm) for 20 min. In the second step, 1-6 wt% Ag/MSS samples (600 mg) with Cpt/MSS ratio of 0.05 was allowed to stir overnight in ice cool environment. The

Table 1
List of different wt% Ag loaded MSS and 4 wt% loaded Ag on different structured nanocarriers using wet impregnation technique.

Samples	Ag loading	Support	Product	Cpt/nanocarrier	Final product
1	1 wt%	MSS	1Ag/MSS	0.05	1Ag/MSS/Cpt
2	2 wt%	MSS	2Ag/MSS	0.05	2Ag/MSS/Cpt
3	4 wt%	MSS	4Ag/MSS	0.05	4Ag/MSS/Cpt
4	6 wt%	MSS	6Ag/MSS	0.05	6Ag/MSS/Cpt
5	4 wt%	SBA-16	4Ag/SBA-16	0.05	4Ag/SBA-16/Cpt
6	4 wt%	TiZSM-5	4Ag/TiZSM-5	0.05	4Ag/TiZSM-5/Cpt
7	4 wt%	Mesosilicalite	4Ag/Mesosilicalite	0.05	4Ag/Mesosilicalite/Cpt
8	4 wt%	Halloysite	4Ag/Halloysite	0.05	4Ag/Halloysite/Cpt
9	4 wt%	Silicalite	4Ag/Silicalite	0.05	4Ag/Silicalite/Cpt

*The Cpt/nanocarrier ratio corresponds to 15 mg of Cpt loading on 300 mg of nanocarrier.

solution was then filtered, washed with 5 mL of normal saline and dried at room temperature using vacuum drying method. The filtrate was then analyzed by UV–visible spectroscopy at 208 nm. Prior to analysis, a calibration curve was established at λmax = 208 nm. The analysis of 4 wt% Ag/MSS/Cpt showed a DEE % of 90 % and DLC % of 4.34 %. The drug Cpt entrapment efficiency (DEE%) and loading capacity (DLC%) were measured as:

$$DEE(\%) = \left[\left(\frac{Initial\ amount\ of\ Pt\ -\ Pt\ in\ filtrate}{Initial\ amount\ of\ Pt}\right)\right] \times 100$$

$$DLC(\%) = \left[\left(\frac{Initial\ amount\ of\ Pt\ -\ Pt\ in\ filtrate}{Pt + MSS}\right)\right] \times 100$$

2.3. Characterization techniques

The phase of 1-6 wt% Ag/MSS and 4 wt% Ag/structured silica were analyzed using benchtop XRD (Miniflex 600, Rigaku Co., Tokyo, Japan). The surface area, pore volume with pore size distribution modifications before and after Ag addition were measured using the nitrogen adsorption technique (ASAP-2020 plus, Micromeritics Instrument Corp., Norcross, GA, USA). The silver nanoparticle chemical coordination was analyzed using DRS-UV–visible spectroscopy analysis (JASCO Corporation, Hachioji-City, Tokyo, Japan). The chemical compositions and oxidation states of the elements in 1Ag/MSS and 6Ag/MSS were studied using Kratos DLD XPS instrument, where C1s peak at 284.8 eV is used as a reference to calibrate the XPS spectra. The hydrodynamic particle size, polydispersity index, and zeta potential of MSS, 1, 4, and 6Ag/MSS samples were measured by Zetasizer Nano ZS (Malvern Panalytical Ltd, Worcestershire, UK). The sample (5 mg) was mixed with 10 mL of PBS buffer (pH 7.4) and sonicated for 30 min. The sample was then transferred into a disposable measuring cell and analyzed. The measurement was carried out three times at room temperature. SEM was analyzed using JSM-6610LV from JEOL Ltd, Tokyo, Japan. Elemental mapping was obtained by energy dispersive spectroscopy (EDS) using Aztec software (Oxford). The morphology of the sample was analyzed using transmission electron microscopy (JEM2100F from JEOL Ltd, Tokyo, Japan).

2.4. In vitro Cpt release study

The drug release analysis of Ag loaded nanoformulations such as 1-6 wt% Ag/MSS, 4 wt% Ag loaded SBA-16, TiZSM-5, Mesosilicalite, Halloysite and Silicalite was studied by Franz cells (PermeGear, USA) (Balasamy et al., 2019). The system was assembled with tumor acidic solvent reservoir, 8 inline cells, solution driving peristaltic pump and sample collector. The setup was constantly maintained at 37 °C using water heater (Julabo GmbH). Firstly, dialysis membrane (MWCO = 14000, Sigma) was activated by washing in phosphate buffer solution. Any air blockages in the tubings were removed by purging with phosphate buffer solution. One square inch sized membrane was placed inside the Franz cells. The Ag loaded nanoformulation was mixed with acidic PBS solution (30 mg/mL) and then placed in the donor site. Then the solution was pumped at the constant volume flow rate of 10 mL/60 min with volume to time ratio of 0.167. The samples were collected at every hour, analyzed and quantified by Cpt calibration curve using JASCO UV–Vis spectroscopy. The release study using each nanoformulation was studied in triplicate.

2.5. Anticancer studies

2.5.1. MTT assay

Human colorectal carcinoma (HCT-116) and human cervical cells (HeLa) were used to study the cell viability. Embryonic kidney cells (HEK-293) was used to evaluate the cytotoxic of the samples considered as normal cells. The following materials, streptomycin (1 %), DMEM, penicillin, FBS (10 %), L-glutamine (5 %), and Se_2Cl_2 (1 %) were used for cell culture. Cell lines were purchased from ATCC (American Type Culture Collection), Manassas, Virginia, United States. 96 well plates were used for cell culture and kept in 5 % CO_2 incubator (Thermo Fisher Scientific, Inc., Waltham, MA, USA) at 37 °C. 75–80 % confluence cells used for further study. The cell viability was done by MTT assay as described previously, where effect of nanoformulations was examined on both cancer cells (HCT-116 and HeLa) and non-cancerous cells (HEK-293) (Khan et al., 2018). In brief, 70–80 % confluence cells (HCT-116 and HEK-293) were treated with various doses (5.0 μg to 50 μg/mL) of nanoformulations. In control group, nanoformulations were excluded and after 48 h, the cells were incubated in MTT (Sigma Aldrich, St. Louis, MO, USA) for 4 h. The control and nanoformulations treated groups were used for the MTT assay (5 mg/mL). The treated cells were kept in CO_2 incubator for 4 h. After changing the cell culture media with DMSO (1 %), cells were examined under ELISA plate reader at 570 nm (Biotek Instruments, USA). The percentage of cell viability was calculated for the statistical analysis. ANOVA were used to analyse the data. All the analysis was run on GraphPad Prism software. P value less than 0.05 was taken as significant difference in results.

2.5.2. Apoptotic effect of nanoformulations using DAPI staining

We have examined the effect of nanoformulations on cancer nuclei to confirm that cancer death is due to apoptosis process. In the present study we have used DAPI (4′,6-diamidino-2-phenylindole) to examine the cancer cell DNA after the treatments. DAPI is a fluorescent stain that binds strongly to A-T-rich regions in DNA. DAPI is a blue-fluorescent DNA stain that exhibits ~ 20-fold enhancement of fluorescence upon binding to AT regions of dsDNA. Because of its high affinity for DNA, it is also frequently used for counting cells, measuring apoptosis, sorting cells based on DNA content, and as a nuclear segmentation tool in high-content imaging analysis. The morphology changes of cancer nuclear structure due to treatments of nanoformulations were examined by DAPI staining assay. Cells were divided into two groups, in which the control group was without nanoformulations. Whereas, in the experimental group, nanoformulations (25 μg/mL) were added. The cells after 48 h of treatment was subjected to ice cold paraformaldehyde (4 %) and Triton

X-100 in PBS. Then DAPI (1.0 μg/mL) for 5 min was used under a dark environment to stain the cells. Followingly, the cells were washed with PBS and cover-slipped. The DNA staining was examined by using Confocal Scanning Microscope (Zeiss, Germany). The data presented as mean (±) standard deviation (SD) obtained from triplicates and one-way ANOVA followed by Dennett's post hoc test with GraphPad Prism Software (GraphPad Software, USA) for final statistical analysis.

2.6. Antibacterial activity

The bacterial strains of *Pseudomonas aeruginosa* ATCC27853 (gram-negative) and *Staphylococcus aureus* ATCC25923 (gram-positive) were subjected to antibacterial studies. The bacteria were sub-cultured and maintained on Muller Hinton agar (MHA). The stock solution of nanomaterial (8 mg mL^{-1}) was sonicated for 10 min in Mueller Hinton broth (MHB) to obtain the homogenized solution for antibacterial assay. Inoculum was prepared by adjusting the cell number to 1.5×10^8 CFU mL^{-1} by using freshly grown strains grown for overnight at 37 ℃.

2.6.1. Broth dilution method

The minimum inhibitory/bactericidal concentration (MIC/MBC) of the synthesized nanomaterial was obtained by applying the broth dilution method (Baig et al., 2020). Briefly, 1 mL of sterile MHB with the varying concentration of nanomaterial starting from 8 mg/mL to 250 μg/mL was formulated except $AgNO_3$ (0.125 to 0.0038 mg/mL). About 100 μL of the adjusted inoculum was inoculated into each tube and were further incubated for 24 h (at 37 °C) with agitation of 120 rpm. A control tube of bacteria without nanomaterial was included as control. The following day 10 μL from the tubes were streaked on freshly prepared MHA plates and further incubated at the conditions mentioned above. After the completion of incubation duration, the plates were recorded for MIC and MBC. MIC was taken as the lowest concentration of nanomaterial that inhibited 90 % of the bacterial growth, whereas MBC was recorded as the lowest concentration that completely destroyed the bacterial cells or had CFU less than three. The data were presented as mean standard deviation obtained from triplicates with *P-value significant is 0.05.

3. Results and discussion

3.1. X-ray diffraction and nitrogen adsorption–desorption isotherm

The monodispersed spherical silica with different weight percentages of Ag nanoparticles loadings were characterized by X-ray diffraction (XRD) and N_2 adsorption–desorption technique (Fig. 1a-i). Fig. 1(a-d) shows the X-ray diffraction pattern of 1-6 wt% Ag/monodisperse spherical silica. 1Ag/MSS showed only the broad diffraction pattern with peak height at $2\theta = 22.5^\circ$ characteristics to that of the (1 0 1) plane of amorphous silica. With 2, 4, and 6 wt% loadings, Ag nanoparticles corresponding to the cubic phase were observed with (1 1 1), (2 0 0) and (2 2 0) planes. The nitrogen adsorption–desorption technique was used to study the textural variation (surface area, pore size, and pore volume) of support MSS and Ag impregnated samples (1, 2, 4 and 6 wt% Ag/MSS) (Fig. 1e-i). MSS sample showed a type IV isotherm with hysteresis loop pattern at higher relative pressure $p/p_0 > 0.8$. The parent silica showed a uniform pore size distribution with a high surface area of 170 m^2/g and pore volume of 0.35 cm^3/g. The Ag impregnated samples showed a decrease in the volume of nitrogen adsorption compared to MSS indicating a reduction in the surface area and pore structure. For instance, the loading of 2 wt% Ag attributes to 67 % decreases in surface area of MSS to about 56 m^2/g. Similarly, a 20 % reduction in the total pore volume of 0.28 cm^3/g was observed compared to MSS. These results suggest that the surface area and pores of MSS are accessible for Ag NPs. Further, increasing the Ag loading to 6 wt% had a significant drop in the surface area to about 90 % (17 m^2/g) along with pore volume (0.08 cm^3/g). However, the average pore diameter of MSS was about 8.3 nm increases with Ag loading to about 20 nm. Yu et al., (2022) have observed that Ag_2O loading on MCM-41 increases the pore diameter compared to support MCM-41 and is attributed to the stacking of silver oxide NPs at the interior and exterior side of the pore channels. In our case, a similar pore expansion shows the deposition of AgNPs at the external pore walls of MSS and contributes to the increase in the pore size.

3.2. In vitro drug release

The release ability of Cpt with increasing Ag loadings over MSS was carried out in a continuous flow system that imitate *in vitro* drug release (Fig. 2a and b). The system is more accurate than that of using a dialysis membrane, which is a closed system. In this condition, sink and

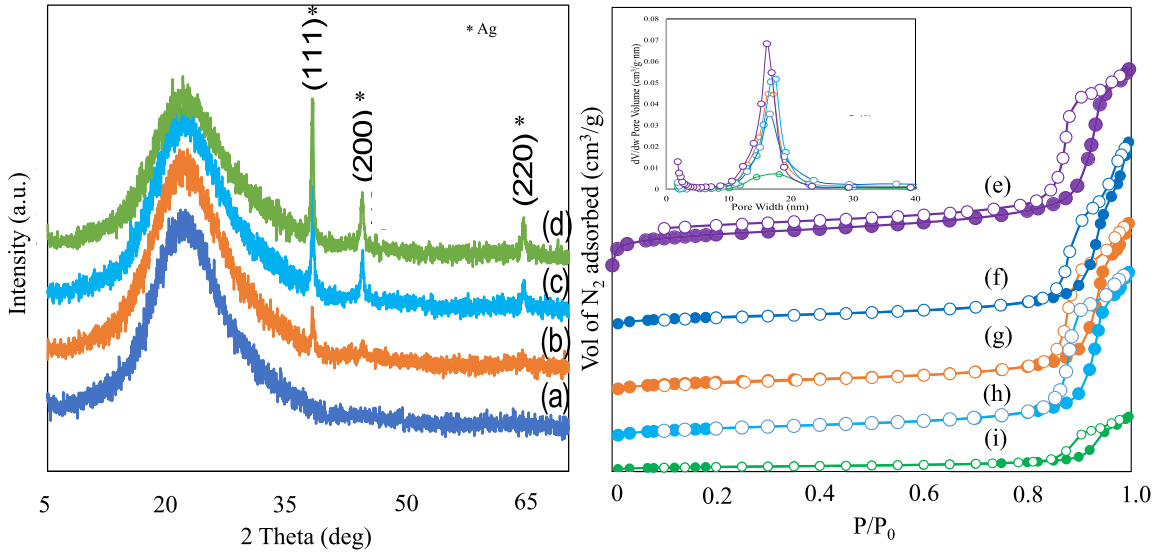

Fig. 1. X-ray *diffraction* of 1-6 wt% Ag loaded monodispersed spherical silica (a) 1Ag/MSS, (b) 2Ag/MSS, (c) 4Ag/MSS and 6Ag/MSS, N_2-adsorption–desorption isotherm of (e) MSS, (f) 1Ag/MSS, (g) 2Ag/MSS, (h) 4Ag/MSS and (i) 6Ag/MSS.

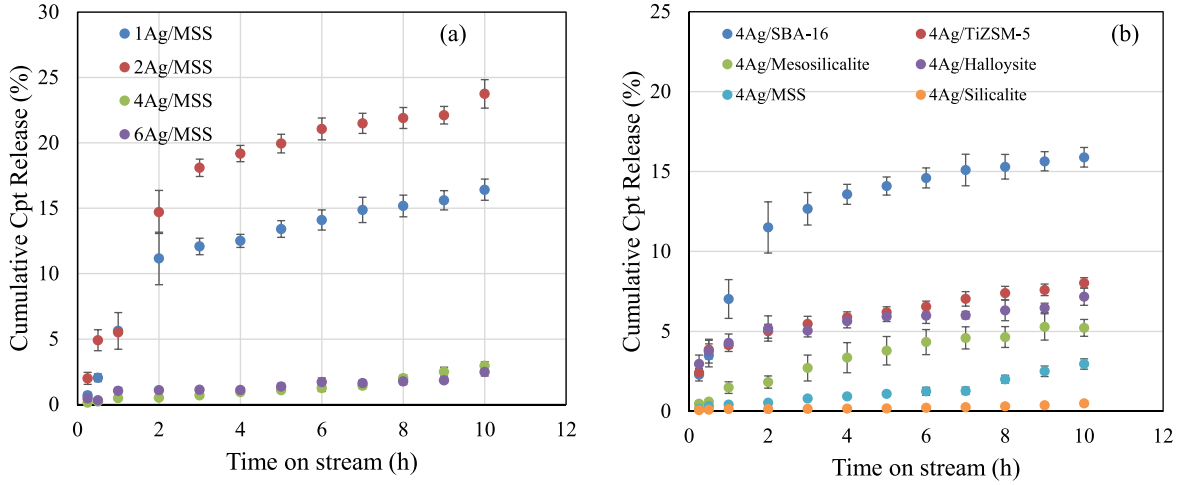

Fig. 2. (a) *In vitro* Cpt release over 1-6Ag/MSS and (b) 4Ag impregnated on different porous structured materials using automated Franz cell system for 10 h.

saturation levels were negated due to an open system (continuous flow of buffer solution). The removal and refilling errors were reduced due to semi-automation. The release profiles were reproduced with triplicate runs. In the case of Cpt release (Fig. 2a), the percentage cumulative Cpt release shows the following pattern 2Ag/MSS > 1Ag/MSS > 4Ag/MSS >6Ag/MSS. The quick release of drugs is used for acute diseases, while slow and sustained release is beneficial for cancer therapeutics (Senapati et al., 2018). Such controlled slow release to cancer cells, reduce the toxic effect on normal cells. Interestingly, the cumulative percentage release pattern as observed in Fig. 2a showed an inverse relation with respect to different weight percentage Ag loading. A quick release of Cpt occurs at lower Ag loadings (1 wt% and 2 wt%) on MSS, whereas the release of Cpt reduced significantly with high Ag loadings (4 wt% and 6 wt%). Therefore, 4 wt%Ag loading was chosen due to sustained release and compared with 4 wt% Ag loaded on different structured materials. The release profile over different structured silica shows that SBA-16 with cubic-shaped pores have high Cpt release (~15 %) within short duration between 0 and 10 h. TiZSM-5 zeolite with micropores, halloysite with nanotube, and mesosilicate with mesopores showed an intermediate Cpt release (3–5 %). In the case of 4 and 6Ag loading on MSS, Cpt remains intact, which indicates a synergistic interaction between Ag and Cpt complex (Fig. 2b).

The stability experiments of two samples (1 and 4Ag/MSS) were studied for the period of 72 h (dialysis membrane) at pH 5.6 and 6.6, respectively. In our previous study, structured silica such as SBA-16 functionalized with 3-aminopropyltriethoxysilane and polyacrylic acid showed a high percentage cumulative Cpt release at about 60 % (Alomari et al., 2019). Chitosan-modified spinel ferrite/spherical silica nanocomposites also showed similar release profile ranging between 60 and 70 % (Jermy et al., 2020). In this study, 1Ag/MSS showed a maximum Cpt release reaching about 12.7 % for 72 h, while 4Ag/MSS showed a further slow release of about 8 % for 72 h. A high Cpt release at lower Ag loading, while a slow and sustained Cpt release with high Ag correlates with release trend of Franz cell system (Table 2). Increasing the pH 6.6, the Cpt release over 1Ag/MSS increases to a maximum of 33.24 % for 72 h, while with high 4Ag/MSS slightly improved to 4.26 % %, respectively. The Cpt release profile (Fig. 2) and Table 2 clearly show such interactive and release abilities between Ag and Cpt. This evidence indicates that different amount of Ag interacts differently with Cpt. The higher the Ag species, the lower the Cpt release and *vice versa*.

3.3. Kinetics of drug release using Korsmeyer-Peppas model

The drug release profiles were examined using the Korsmeyer-Peppas model, expressed using the equation:

$$R\% = kt^n$$

where R% is the drug percentage release at time (t), k and n are the kinetic rate constant and the release exponent, respectively. The ob-

Table 3
Fitting parameters for drug release.

Nanoformulations	k	n	R^2
1Ag/MSS	3.6847 ± 1.3179	0.7733 ± 0.1932	0.8883
2Ag/MSS	6.5929 ± 1.4536	0.6415 ± 0.1259	0.9280
4Ag/MSS	0.3831 ± 0.0748	0.7471 ± 0.1127	0.9562
6Ag/MSS	0.7261 ± 0.1591	0.4473 ± 0.1255	0.8631
4Ag/SBA-16	5.8467 ± 1.0390	0.5158 ± 0.1034	0.9252
4Ag/TiZSM-5	4.0534 ± 0.2357	0.2848 ± 0.0357	0.9693
4Ag/Mesosilicalite	1.2038 ± 0.1264	0.6840 ± 0.0631	0.9832
4Ag/Halloysite	4.1887 ± 0.1615	0.2088 ± 0.0239	0.9743
4Ag/MSS	0.4088 ± 0.0855	0.7086 ± 0.1200	0.9454
4Ag/Silicalite	0.1266 ± 0.0283	0.4000 ± 0.1274	0.8304

Table 2
in vitro Cpt drug release over 1Ag/MSS and 4Ag/MSS.

Time (h)	(pH = 5.6) 1 wt% Ag/MSS		(pH = 6.6) 1Ag/MSS		(pH = 5.6) 4Ag/MSS		(pH = 6.6) 4Ag/MSS	
	Cpt Release (mg)	Cum. Release (%)	Cpt Release (mg)	Cum. Release (%)	Cpt release (mg)	Cum. Release (%)	Cpt release (mg)	Cum. Release (%)
1	1.36	5.25	4.89	18.80	0.69	2.66	0.25	0.98
6	2.30	8.84	6.55	25.20	1.32	5.06	0.41	1.57
12	2.55	9.82	7.04	27.10	1.67	6.43	0.54	2.06
24	2.75	10.57	7.75	28.83	1.73	6.66	0.79	3.04
48	2.79	10.73	8.37	32.20	1.91	7.35	1.01	3.89
72	3.31	12.72	8.64	33.24	2.04	7.84	1.11	4.26

tained fitting parameters together with their 95 % confidence intervals and correlation coefficient (R^2) are shown in Table 3. The drug release profiles were also examined using different models including zero order, first order and Higuchi model, expressed using the equations:

Zero order:

$$C_t = C_\infty + kt$$

First order:

$$ln(C_t/C_\infty) = kt$$

Higuchi model:

$$C_t/C_\infty = k(t)^{0.5}$$

where C_t is the cumulative amount of drug released at time t, C_∞ is the cumulative amount of drug released at infinite time. The drug release constant (k) and the correlation coefficient for the models are presented in Table S2.

For the different loadings of Ag on MSS support, the rate of drug release as observed from the release constant (k) is higher at low Ag loadings (1 wt% and 2 wt%). Also, the diffusion mechanism at all loadings followed the non-fickian diffusion mechanism ($0.45 < n < 0.89$) except at 6 wt% loading that is slightly less than 0.45 ($n = 0.4473 < 0.45$). Similarly, for the different loadings of Ag on different supports (SBA-16, Ti-ZSM-5, Halloysite, Mesosilicalite, MSS, and silicalite), both the release constant (k) and the release exponent (n) showed different values signifying that the rate of drug release and diffusion mechanism (fickian or non-fickian) depends on the nature of the support. All the models have correlation coefficient in the range of $0.75 < R2 < 1$, depending on the drug formulations. However, among all the models, Korsmeyer-Peppas model still gave the best correlation coefficient for all the formulations. The regression correlation coefficient (R^2) is high for the different loadings and different supports, implying that, the Korsmeyers-Peppas model appropriately describes the drug release kinetics.

3.4. Diffuse reflectance UV–Visible spectroscopy (DR-UV Vis)

DR-UV Vis is used to characterize the oxidation state of transition metals. In the present study, the coordination state of different weight percentages of Ag (1-6 wt% Ag) before and after Cpt functionalization was shown in Fig. 3(a-h). In the case of Ag/MSS nanoformulations, Ag^+, $Ag_n^{\delta+}$ (nano-sized clusters), and Ag^0 species at 220 nm, 300 nm, and 400 nm were observed (Aldossary et al., 2022). After the introduction of Cpt, an increase in the absorption band towards the visible region occurred at 221, 268 nm and 400 nm, indicating the presence of tetrahedral, octahedral and polymeric Pt species (Gharibshahi and Saion, 2012, Jermy et al., 2018). In the case of 2, 4, and 6 wt% Ag loading, the intensity of the Ag^0 band increases indicating the presence of Ag^0 nanoparticles. Such bands are primarily attributed due to presence of free electrons giving rise to surface plasmon resonance. Conversely, the cisplatin peak intensity band in Cpt reduced with increasing Ag content exhibiting the presence of an effective cohabitation of Pt in Cpt with dominant Ag nanoparticles. The synergistic presence of Pt of Cpt and Ag nanoparticles indicates a dispersion and cohabitation of Pt and Ag nanoparticles on MSS. Fig. S3(a and b) represents the XPS analysis of elemental, binding energy and chemical state of 1Ag/MSS and 6Ag/MSS. The survey spectrum depicts the elements and atomic ratio of 1Ag/MSS and 6Ag/MSS. The high-resolution spectra were presented the energy scan for all elements. The C1s peak at 285 eV was composed of two peaks at binding

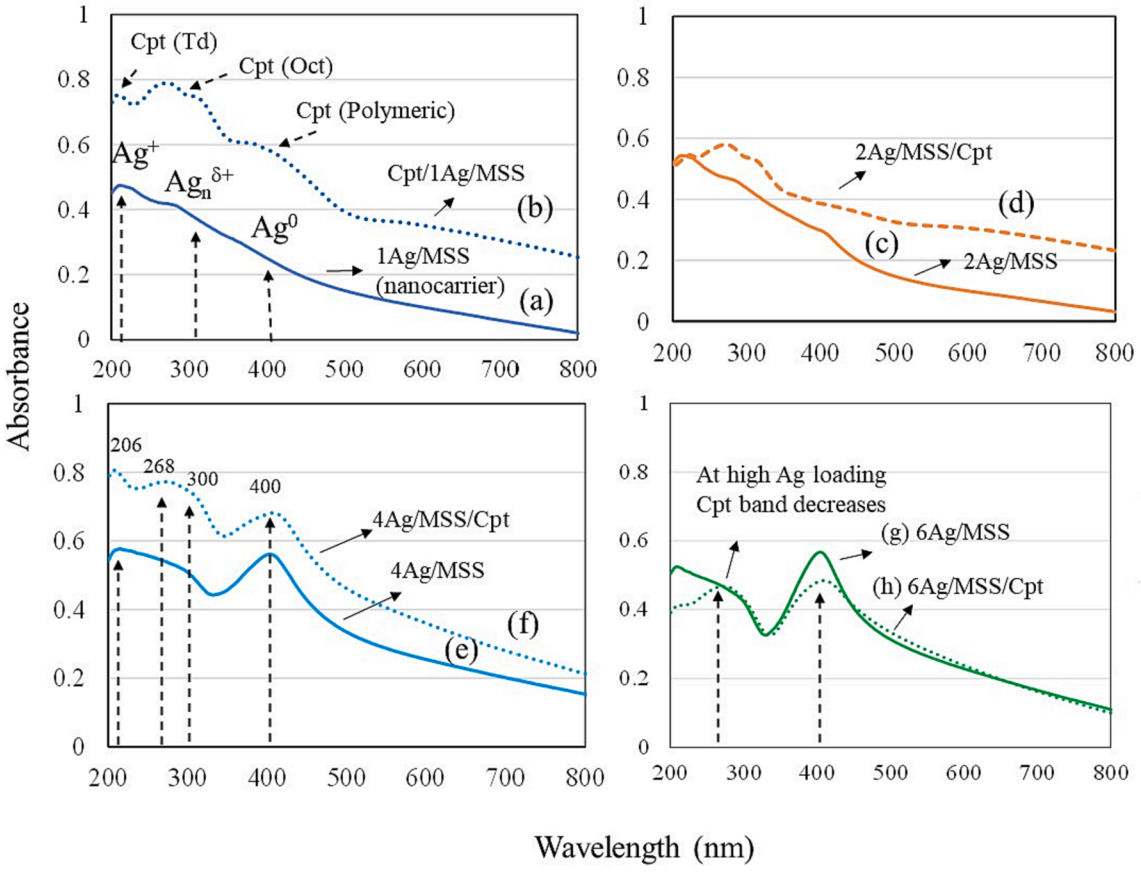

Fig. 3. DR-UV Visible spectra of 1-6 wt% Ag/MSS and 1-6 wt% Ag/Cpt containing monodispersed spherical silica (a) 1 wt% Ag/MSS, (b) 1 wt% Ag/MSS/Cpt (c) 2 wt % Ag/MSS, (d) 2 wt% Ag/MSS/Cpt, (e) 4 wt% Ag/MSS and (f) 4 wt% Ag/MSS/Cpt, (g) 6 wt% Ag/MSS and (h) 6 wt% Ag/MSS/Cpt.

energy of 284.8 eV and 286.7 eV which related to C = O as depicted in Fig. S3(a and b) (Avishek Roy et al., 2019). The O spectrum in both compositions showed only one peak O 1 s at 532.6 and 532.4 eV. The O 1 s peak shows a slight shift when increasing the loading of Ag due to Fermi level of oxide (Dalby et al., 2007). The fitted spectra of Si 2p showed deconvoluted of four peaks at 103.0, 103.4, 103.5 and 103.8 eV relevant to oxidized silicon which indicated to Si^{4+} (Hellen S. Santos et al., 2022). Furthermore, the peak Si 2p intensity increased when increasing the Ag loading. The Ag 3d peaks at 368.4 and 374.5 eV denoted to Ag 3d5/2 and Ag 3d3/2 respectively as seen in Fig. S3(a and b) which respect to the metallic silver. The Ag 3d3/2 deconvoluted to 374.1 and 374.8 eV (Nienke J. Firet et al., 2019).

3.5. SEM-EDS analysis

The Ag and Cpt distributions of 1 wt% Ag/Cpt/MSS and 4 wt% Ag/Cpt/MSS samples were mapped using SEM-EDS analysis (Fig. 4a-i). The elemental mapping pattern shows the well-distributed Ag and Cpt species at 1 wt% loading over MSS (Fig. 4a-c). EDS spectra showed the presence of Si, Ag, and Pt of Cpt (Fig. 4d and e). The densification of both species was revealed as Ag loading increases with 4 wt%. Some agglomerations are observed which can be attributed to the cohabitation of Ag and Cpt species leading to some formation of large grains (Fig. 4f-i). SEM-EDX and zeta potential (Table S1) indicate the agglomeration of Ag-Cpt complex and heterogeneity signaling a unique role played by Ag at high loading over MSS. Li et al., (2005) has stated that in Pt-Ag/SiO_2 nanocomposite, co-existence of linear and bridged Pt species occurs. The presence of Ag on the Pt/SiO_2 catalyst changes the Pt surface structure. The Ag enrichment occurs at the catalyst surface and reduces the Pt concerted activities (ensembles). Further, the oxidation property of Pt is also altered with Ag addition. In our study, there exists a multispecies cohabitation and synergistic action between the content of Ag and Pt of Cpt (Figs. 2 and 4).

3.6. High-resolution transmission electron microscopy (HR-TEM)

HR-TEM was used to investigate the effect of 1 and 6 wt% Ag loadings and Pt of Cpt dispersion on MSS. In the case of 1 wt% Ag/MSS/Cpt sample, the monodispersed spherical silica form is retained with a uniform particle size of about 80 nm without any distinct Ag and Cpt nanoparticles on MSS. (Fig. 5a). However, the morphological analysis of 6 wt%Ag/MSS/Cpt at the microscopic level clearly shows the large Ag particles with an average size of about 8 nm was dispersed on MSS (Fig. S1). Interestingly, Pt nanoparticles of Cpt with a particle size of about 3.3 nm were observed as nanosized aggregation around large Ag particles on MSS (Fig. 5b-d). The variation in the Pt particle distributions with increasing Ag content from 1 to 6 wt% clearly shows the cohabitation effect of Ag on Pt species. Moreover, the lattice fringes of Ag and Pt were processed using HRTEM (Fig. 5d and Fig. S4). The larger Ag nanoparticles were confirmed with the lattice d-spacing of 0.24 nm corresponding to the (1 1 1) plane of face-centered cubic crystal structure (Fig. 5d). The smaller Cpt nanoparticles illustrate the d-spacing of

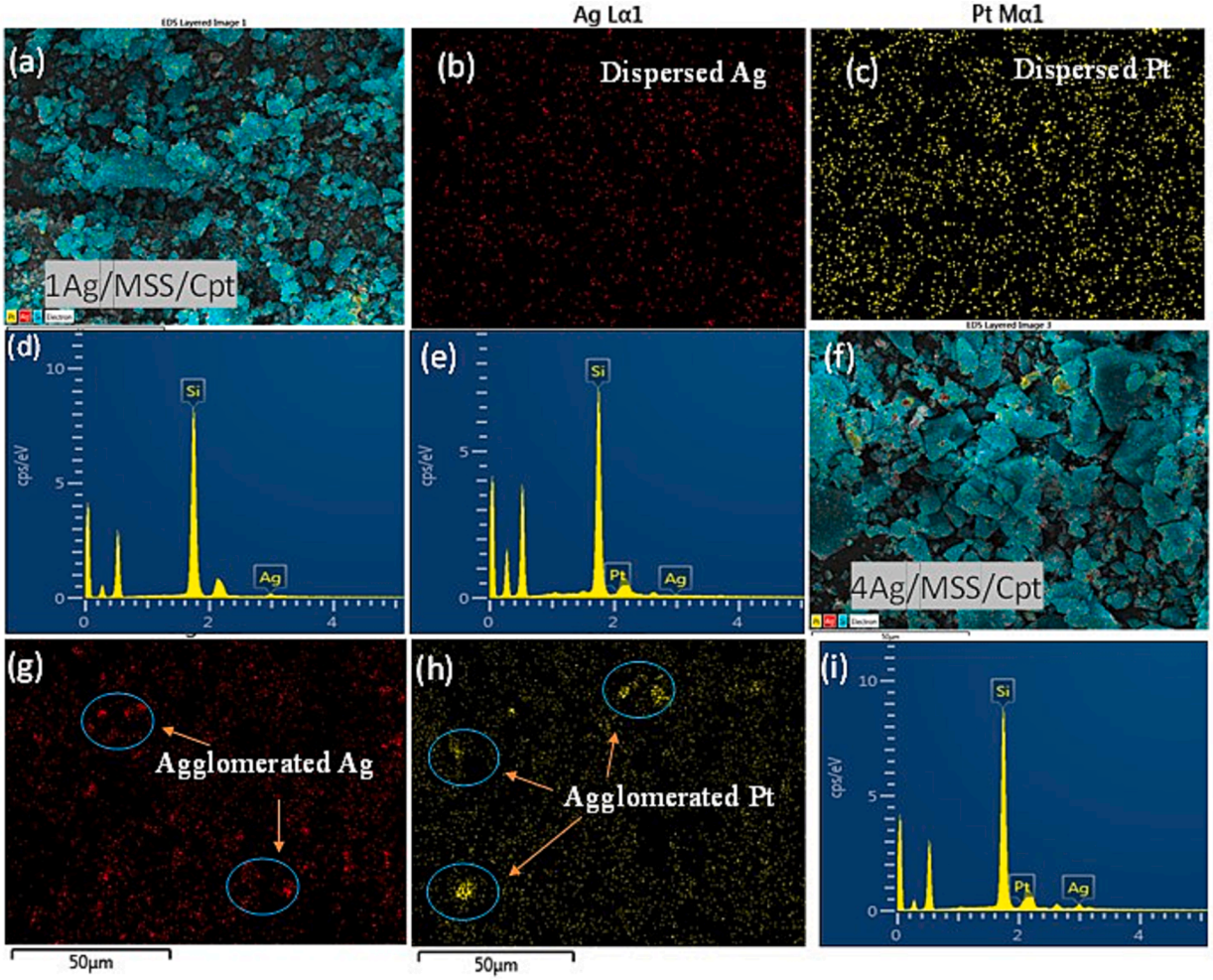

Fig. 4. SEM-EDS analysis of (a) 1Ag/MSS/Cpt, (b and c) elemental mapping of elements Si, Ag, and Cpt, (d and e) EDS spectrum of 1Ag/MSS and 1Ag/MSS/Cpt. SEM-EDS analysis of (f) 4Ag/MSS/Cpt, (g and h) elemental mapping of elements Si, Ag, and Cpt, (i) EDS spectrum of 4Ag/MSS/Cpt.

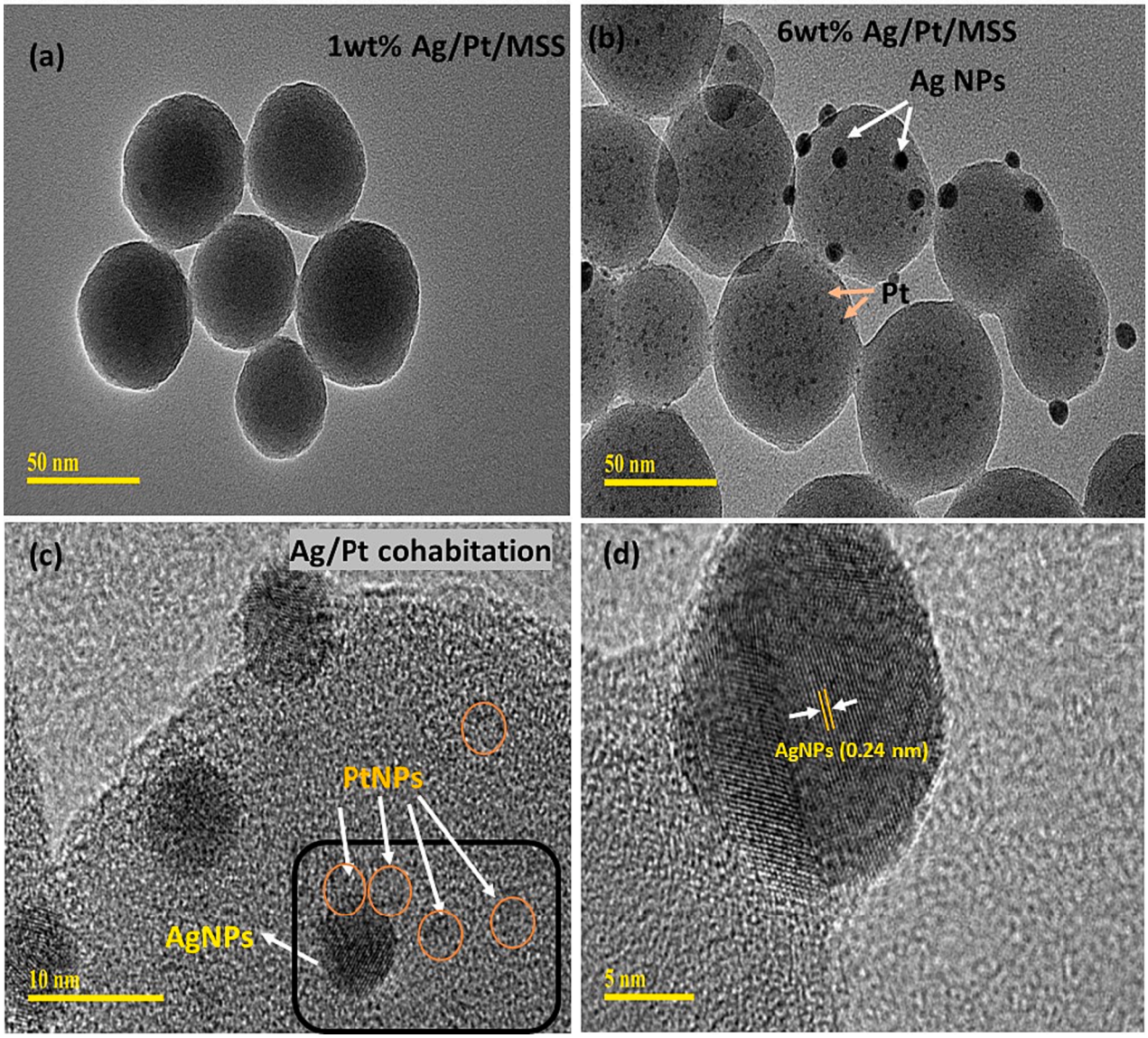

Fig. 5. HR-TEM images of (a) 1 wt%Ag/MSS/Cpt and (b-d) 6 wt% Ag/MSS/Cpt at magnification scale of 50, 10 and 5 nm, respectively.

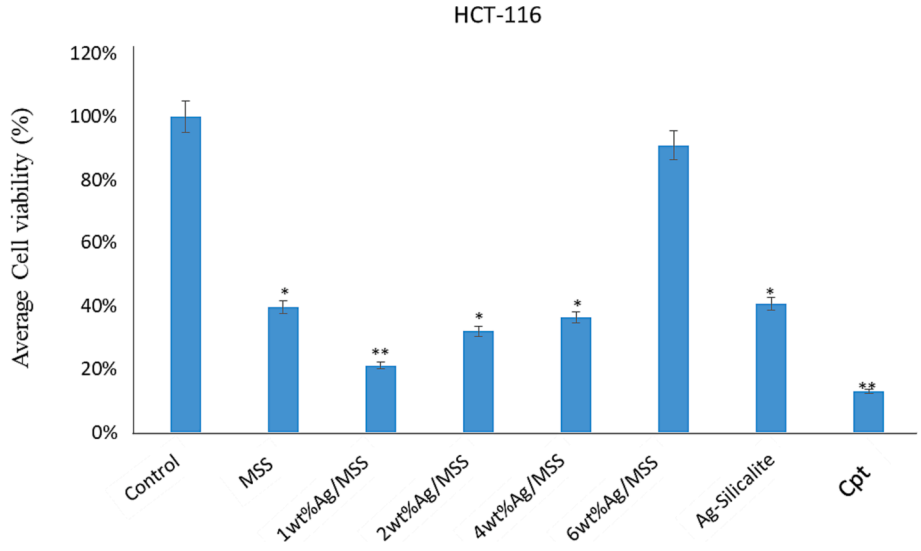

Fig. 6. Cell viability by using MTT Assay: It shows the impact of treatment of nanoparticles on HCT-116 cells post 48-h treatment. * $p < 0.05$; ** $p < 0.001$.

0.22 nm. In Addition, Ag also displayed an inter-fringe distance of 0.22 nm (Fig.S4). The presence of such narrow inter-fringe distance of Ag indicates an effective alloying formation with adjacent lattice plane of bimetallic nanoparticles (Wang et al., 2011).

3.7. Anticancer activity

MTT assay was used to evaluate the cell viability. The influence of different weight percentage Ag loadings on MSS at constant Cpt functionalization over cancer cells such as HeLa and HCT-116 and normal cells embryonic kidney cells (HEK-293) were studied (Figs. 6 and 7). The normal cells were used to evaluate the cytotoxic effect of nanoformulations at the same time HeLa and HCT-116 were used to evaluate the anticancer effect. The impact of nanoformulations on both colon cancer (HCT-116) and cervical cancer (HeLa) cells was examined. The cell viability assay confirmed a significant decrease in the HCT-116 cell viability after the treatments of nanoformulations, except 6 wt% Ag/MSS, where the decrease was not significant (Fig. 6). The cell viability assay confirmed a significant decrease in the HeLa cell viability after the treatments of nanoformulations except Ag-Silicalite, where the decrease was not significant (Fig. 7).

We have also calculated the inhibitory concentration (IC_{50}) of nanoformulations on both HCT-116 and HeLa cells. The IC50 values on HCT-116 cells were MSS (23 μg/mL), 1 wt% Ag/MSS (15 μg/mL), 2 wt% Ag/MSS (21 μg/mL), 4 wt% Ag/MSS (26 μg/mL), 6 wt% Ag/MSS (26 μg/mL), and Cpt (13 μg/mL). Whereas on HeLa cells, IC_{50} were MSS (24 μg/mL), 1 wt% Ag/MSS (13 μg/mL), 2 wt% Ag/MSS (14 μg/mL), 4 wt% Ag/MSS (14 μg/mL), 6 wt% Ag/MSS (15 μg/mL), and Cpt (13 μg/mL). We have also tested the impact of nanoformulations on non-cancerous cells (HEK-293), the average cell viability was 63 % post-treatments (Fig. S2). The cytotoxic impact of NPs post 48 h of treatment was observed and it was found that the average cell viability for Hela cells was 23.22 %, HCT-116 cells was of 43.48 %, and for normal HEK-293 cells, it was 62.00 %. This is the first study demonstrating the cell viability of synthesized nanoformulations against HCT-116 and HeLa cells. We have previously reported the impact of different molecules (nanomaterials and plant extracts) on colon and breast cancer cells (Rehman et al., 2020a). Metal based drug formulation has shown to bypass the drug resistance mechanism involving drug efflux pumps, enzyme (glutathione S-transferases), protein (multidrug resistance-associated protein 1), dysfunction in programmed cell death (apoptosis), alteration in extracellular matrix mechanics, and over expression of hypoxia related protein (hypoxia-inducible factor-1α) (Alavi et al., 2022). AgNPs has been reported to assist in reducing the cancer tissue spread by inhibiting the endothelial cell-specific mitogen (vascular endothelial growth factor) Delivering topoisomerase inhibitor (camptothecin) along with AgNPs is shown to surpass the drug efflux pumps and facilitate apoptosis pathways (Zhan et al., 2017). However, the targeted cellular interaction determines the effectivity of nanoformulations. Based on these observations, we may suggest that synthesized nanoformulations possess an inhibitory effect on HCT-116 and HeLa cells than HEK-293 cells.

3.7.1. Apoptotic cancer cell death

The treatment impact of nanoparticles on HCT-116 cells was studied by staining with DAPI (fluorescent dye) post 48-h treatment. The control cells did not show any inhibitory action on the colon cancer cells (Fig. 8A). However, the treatment of nanoformulations caused a significant decrease in the number of colon cancer cells, as the number of DAPI stained cells was found to be significantly less in the nanoformulations treated cells as compared to control cells (Fig. 8B-H). The decrease in the cancer cells is due to cell death which is due to programmed cell death or apoptosis. In the case of Cpt, a significant number of cancer cell deaths can be observed due to (25 μg/mL) treatment.

The cubic structured SBA-16, TiZSM-5, mesosilicalite, and halloysite showed higher Cpt release than 4 wt% MSS sample. Interestingly, the cell viability study using MTT assay on HCT-116 reflected the drug release pattern, where cell viability decreases in the following pattern 1 wt% Ag/MSS > 2 wt% Ag/MSS > 4 wt% Ag/MSS > 6 wt% Ag/MSS. Ag-silicalite, where Ag is incorporated into the silicalite framework, showed less impact on HCT-116 and HeLa cells. In the case of HeLa cells, 1-6 wt % Ag-loaded MSS nanoformulations were found to be more sensitive with less cell viability percentage and apparent morphological damage which could be owed to cell membrane disruption, nuclear condensation, and fragmentation. Ag nanoparticles tend to inhibit cell viability due to oxidative stress. Ag nanoparticles induced cycle cell arrest and apoptosis to cause cancer cell death in bladder cancer cells (Zhao et al., 2018). Ag nanoparticles conjugated with anti-cancer drug induced apoptosis as confirmed by nuclear condensation, DNA fragmentation, and activation of caspase-3 in A549 cells (Zou et al., 2020). In addition, Ag nanoparticles induced apoptosis in the human hepatocellular carcinoma (HepG2) cell line (Ahmadian et al., 2018). Treatment with normal cells (HEK-293) showed a less cytotoxic effect, reflecting the nontoxic effect of MSS and nanoformulations, irrespective of Ag loadings (Fig. S2). SiO_2 alone shown to exhibit a cytotoxic effect on cancer cells such as hepatocellular carcinoma cells (HCC) and MCF-7 cells. For instance, SiO_2 has been reported to induce apoptosis through p53 and

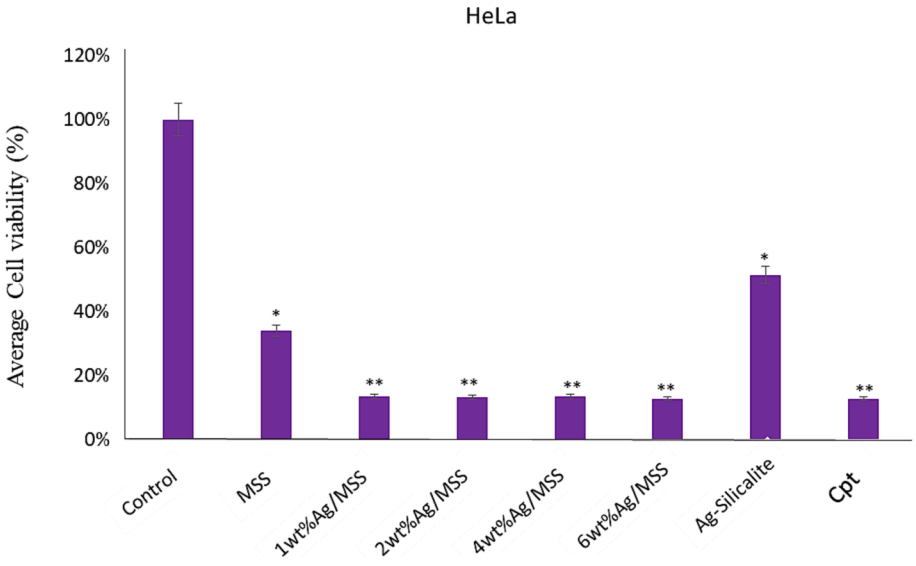

Fig. 7. Cell viability by using MTT Assay: It shows the impact of treatment of nanoparticles on HeLa cells post 48 h treatment. * $p < 0.05$; ** $p < 0.001$.

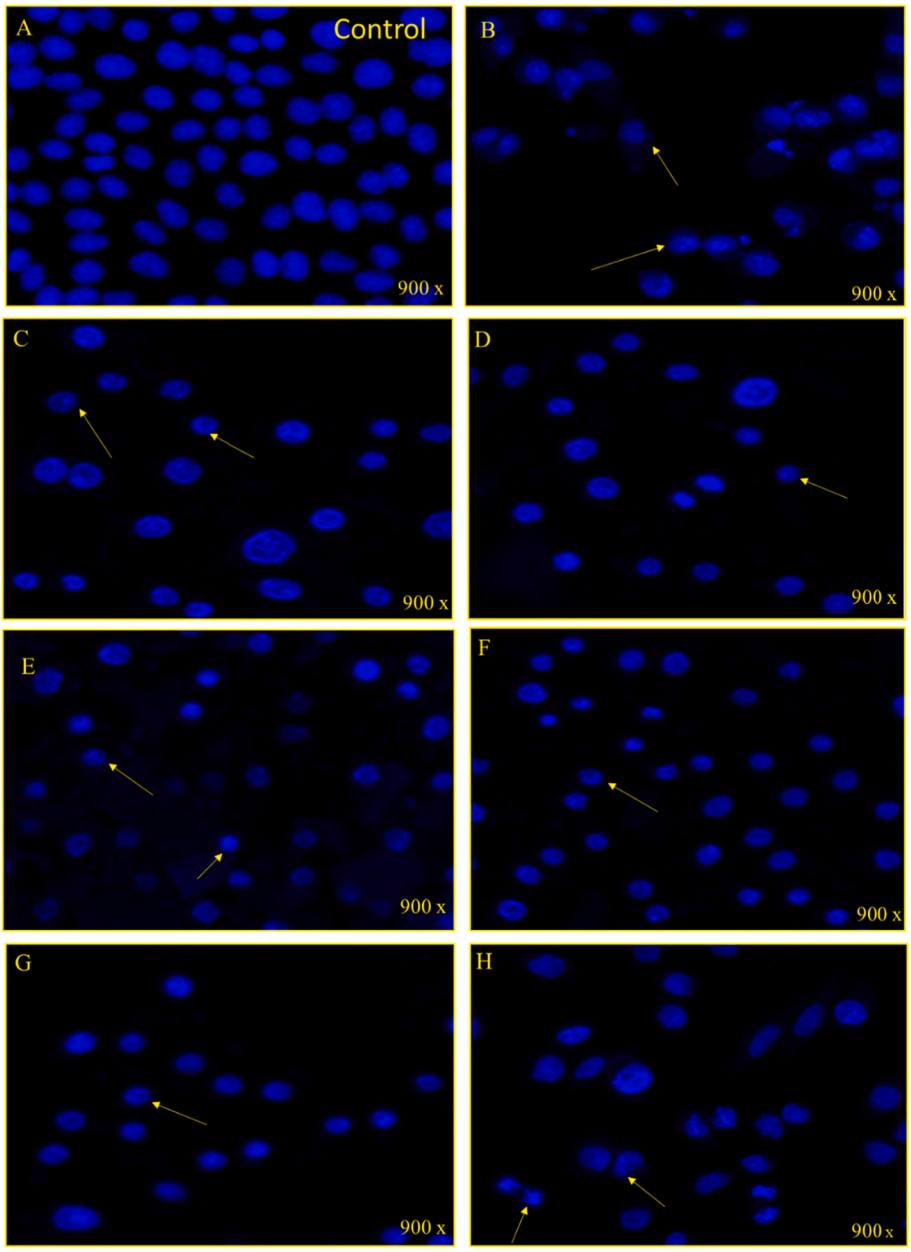

Fig. 8. A-H: Nuclear morphology of HCT 116 cells after stained with DAPI post 48 h treatment. (A) Control cell, (B) (MSS), (C) (1 wt% Ag/MSS), (D) (2 wt% Ag/MSS), (E) (4 wt% Ag/MSS), (F) (6 wt% Ag/MSS), (G) (Ag-silicalite), and (H) (Arrows show the cell membrane disruption, nuclear condensation and fragmentation.

Bax activation mediated by oxidative stress (Niu et al., 2019). The cancer cells with leaky vasculature leads to high silica uptake than normal cells causing subsequent toxic effect to cancer cells (Lin et al., 2006). MSS composed of such SiO_2 has shown to have a similar effect of cancer cells (HCT-116 and HeLa) and less effect on normal cells (HEK-293). Further study with DAPI showed a high cell apoptotic effect with Cpt loading on increased Ag-loaded MSS nanoformulations.

3.8. Antibacterial activity

To demonstrate the antibacterial activity of the nanomaterial, bacterial strains *P. aeruginosa* and S. *aureus* were used. The synthesized nanomaterial depicted the appreciable bactericidal activity with both organism except silica with no inhibitory action. However, *P. aeruginosa was* seen to be slightly more susceptible compared *to S. aureus*. The minimum concentration of nanomaterial for *P. aeruginosa and S. aureus* is presented in Fig. 9 (A and B). The treatments of nanomaterial showed dose-dependent inhibitory action on the bacterial cells. It was observed that the mono dispersed spherical silica with different percentages Ag (1, 2, 4, and 6 wt%) exhibited varying impacts on the bacterial cells. Growth of both the bacteria gram positive and gram negative were inhibited with the increasing percentage of Ag in MSS (Fig. 9 A' and B').

The antibacterial activity of the Ag/MSS nanocomposites with varying Ag loading was evaluated to obtain the mass ratio of Ag NPs. The 6wt%/Ag loading percentage showed the best efficacy with both organisms, which could be due to the dispersion of Ag. The inadequate amount of Ag with only 1 wt%Ag loading showed the least efficacy. The bactericidal action of pure $AgNO_3$, MSS against *P.aeruginosa, and S. aureus.* has been shown in Fig. 9. The MIC/ MBC of all the ratios and $AgNO_3$ showed effectiveness, and the pristine silica showed no antibacterial activity. The bacterial inhibition was regulated by Ag, most

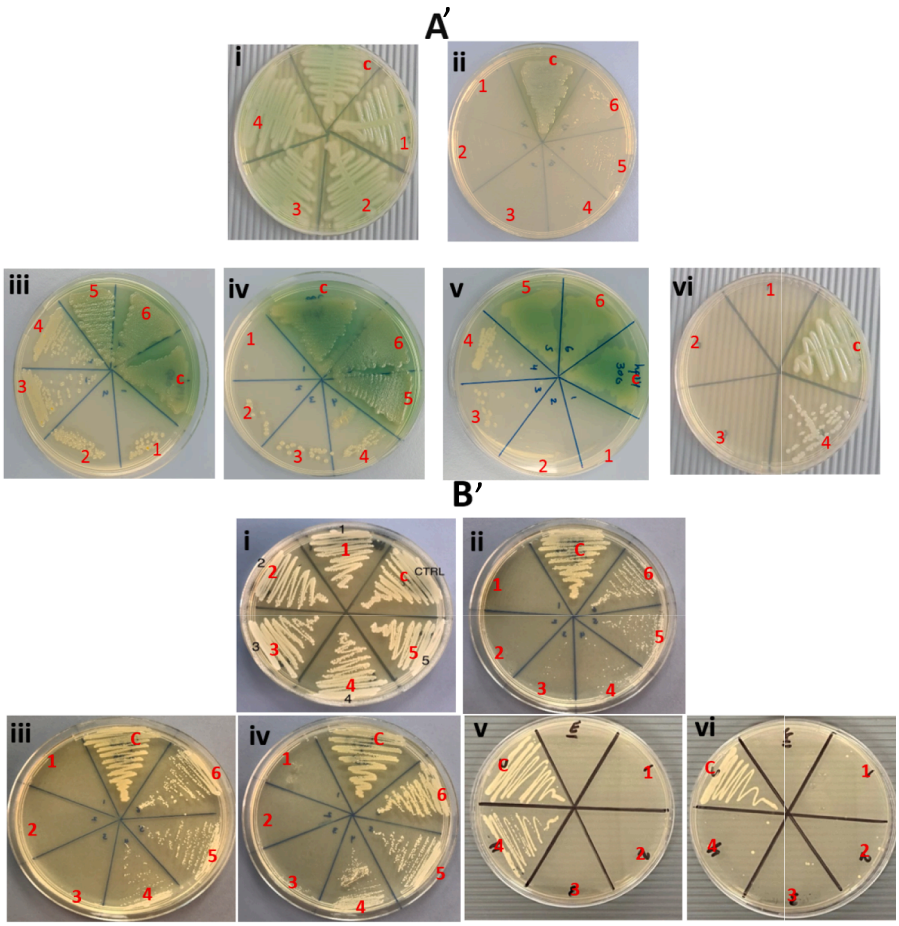

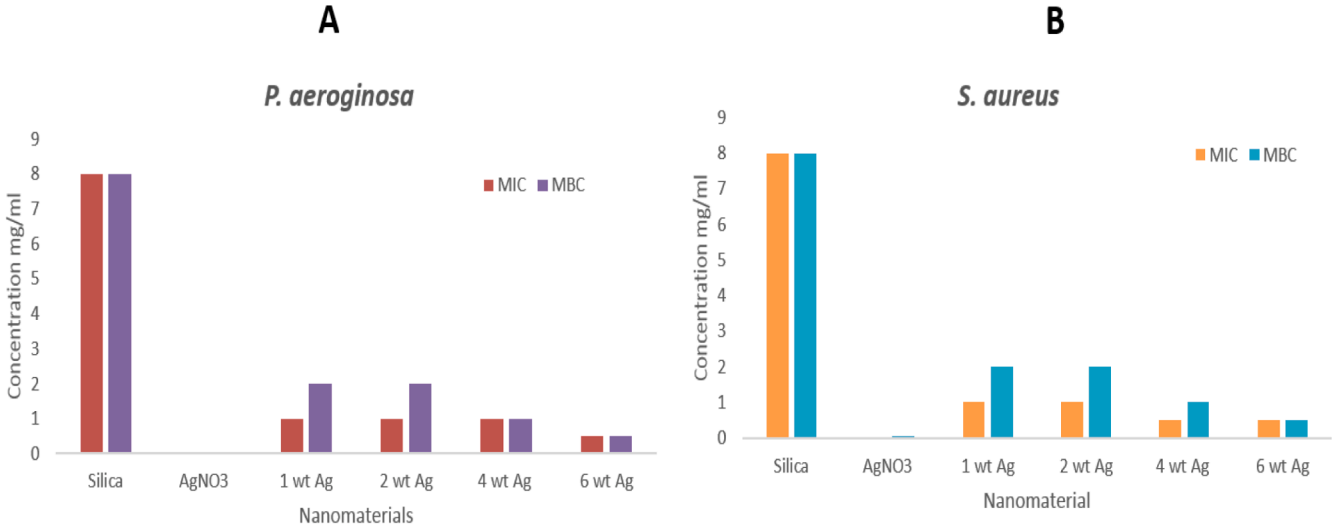

Fig. 9. (A and B). Graph presenting the MIC and MBC values for the Ag/MSS nanomaterials. Fig. 9 (A' and B'). Agar plates showing the MIC and MBC of the synthesized nanomaterial. A': P. aeruginosa, B': S.aureus. i) MSS, ii) $AgNO_3$, iii) 1 wt% Ag/MSS, iv) 2 wt% Ag/MSS, v) 4 wt% Ag/MSS, vi) 6 wt% Ag/MSS [1: 8 mg/mL, 2: 4 mg/mL, 3: 2 mg/mL, 4: 1 mg/mL, 5: 0.5 mg/mL, 6: 0.25 mg/mL, c: control; For $AgNO_3$ i.e., (ii): 1: 0.125 mg/mL, 2: 0.0625 mg/mL, 3: 0.031 mg/mL, 4: 0.155 mg/mL, 5: 0.0075 mg/mL, 6: 0.00387 mg/mL, c: control]. P. aeruginosa growth inhibition MIC (mean = 1.917917, SD = 3.005982), MBC (mean = 2.2525, SD = 2.926011). S. aureus growth inhibition MIC (mean = 1.835833, SD = 3.042319), MBC (mean = 2.260833, SD = 2.918425).

significantly, Ag/MSS nanomaterial indicated an increased antibacterial activity and stability which could be attributed to the Ag introduced. Using one-way ANOVA, the variation in the antibacterial, using varying concentration Ag loading were found significant ($P < 0.001$).

This antibacterial nanocomposite attached to the bacterial cell wall and penetrated into the periplasmic space of bacteria cell, generating reactive oxygen species (ROS) that leads to cellular disorganization. Most studies suggested that nanoparticles significantly attach to the cellular surfaces and produce increased levels of ROS, mainly hydroxyl radicals during the interaction of electrons and water under visible light (Shu et al., 2017). AgNPs are known to possess antimicrobial activity than many antibiotics like vancomycin or gentamicin against pathogens MRSA and P. *aeruginosa* (Mateo and Jiménez, 2022). A significant action of AgNPs was reported against a number of MDR like *E. coli*, *P. aeruginosa*, ampicillin-resistant, and Streptococcus pyogenes (Lara et al., 2010). In the current study, the formulated nanocomposites could have influenced the dispersion and release of Ag and facilitated an efficient contact with the bacterial membrane. The higher dispersion of the nanomaterial could also enhance the surface area, making more ROS production from active sites. It has been shown that Ag/SiO_2 composite can release Ag^+ ions that interact with bacterial cell structure and damage bacterial membrane (Mosselhy et al., 2017). Ag NPs anchored with monodispersed silica promote the damage caused to the cellular surfaces, which could significantly increase the antibacterial and anticancer activity. The current study is crucial for determining the bioactivity mode of operated Ag-monodispersed silica nanocomposites.

In the case of Pt-Ag/SiO_2 nanocomposite, the co-existence of linear and bridged Pt species occurs. The presence of Ag on Pt/SiO_2 catalyst changes the Pt surface structure. Ag enrichment occurs at the catalyst surface and reduces the Pt concerted activities (ensembles). Further, the oxidation property of Pt is also altered with Ag addition (Li et al., 2005). The presence of Pt or Cu with Ag enhances the dissolution of metal species (Ag or Cu), and facilitates a sufficient ion release with improved antibacterial activity (Meister et al., 2022). In our study, there exists a multispecies cohabitation and synergistic action between the content of Ag and Pt of Cpt (Figs. 2 and 4). The electronic transition between Pt surface sites in Pt/bimetallic system is influenced by the inter-atomic distance, coordination and dispersion state (Stamenkovic et al., 2006). Non-alloy metals such as Pt and Ag interactions exhibit a synergistic effect due to their reduction and activation properties. The presence of oxygen functional moieties in the support has the capability to reduce the Pt and Ag salts and increase the bimetal interactions, while the presence of chlorine ions of Pt also increases the mobility of Ag species and interactions with Pt (Chen et al., 2012, Oh et al., 2002). Therefore, the presence of hydroxyl groups of silica could initiate simultaneous reduction and increase the Pt of Cpt with Ag interactions. Moreover, an increase in the Ag content could further increase the bimetal interaction and subsequently control the Cpt release. The Cpt release profile (Fig. 2) and Table 2 clearly show such interactive and release abilities between Ag and Cpt. This evidence indicates that different amounts of Ag interact differently with Pt of Cpt. The higher the Ag species, the lower the Cpt release *vice versa*. In the case of Ag/MSS functionalized with anticancer Pt-based drug such as cisplatin, a controlled release can be beneficial for overcoming drug resistance, facilitating apoptosis pathways, and DNA damage to cancer cells. Antibacterial activity of metal-based nanoformulations is primarily attributed to the ability of release abilities of metal ions that interact with bacterial membrane. The AgNPs and nanocomposite particle shape and size determine the antibacterial activity. AgNPs with particle size ranging between 5 and 10 nm has been reported to induce cell membrane disruption and disintegration of bacterial chromosome. In the present study, Ag impregnated on monodispersed spherical silica able to control the Cpt release, exhibits better antibacterial and anticancer activity (Scheme 1).

4. Conclusion

Metal based hybrid nanoparticles are explored for medical implants coating, diagnostic and targeted cancer therapy. In this study, 1-6 wt% Ag metal nanoparticles impregnated on monodispersed spherical silica has been explored for anti-cancer and antibacterial activity. For comparison, 4 wt%Ag was impregnated on different shaped porous nanocarriers such as SBA-16, mesosilicalite, TiZSM-5, halloysite and silicalite. Physico-chemical characterization revealed that cisplatin release was controlled by the presence of a synergistic cohabitation between Ag (XRD, DRS-UV–visible, SEM-EDX and HRTEM analysis). Zeta potential confirmed the hydrodynamic size and colloidal stability after Ag loadings. The drug delivery study showed a variable Cpt release controlled by the Ag content (1 wt%-6 wt%). The kinetics studies using the Korsmeyers-Peppas model revealed that Ag loading on MSS and on different support materials have pronounced effect on both the rate of drug release and the diffusion mechanism. Anticancer activity using Ag/MSS showed an inhibitory effect on cancer cells (HCT-116 and HeLa cells) than normal HEK-293 cells. AgNPs with monodispersed silica showed excellent antibacterial activity against bacterial strains *P. aeruginosa* and S. *aureus* by promoting damage to the cellular surfaces. Conclusively, MSS can be effectively used to load bioactive metals for multifunctional biomedical applications, especially in treating cancers and bacterial infections.

Funding

Rabindran Jermy would like to acknowledge the funding by

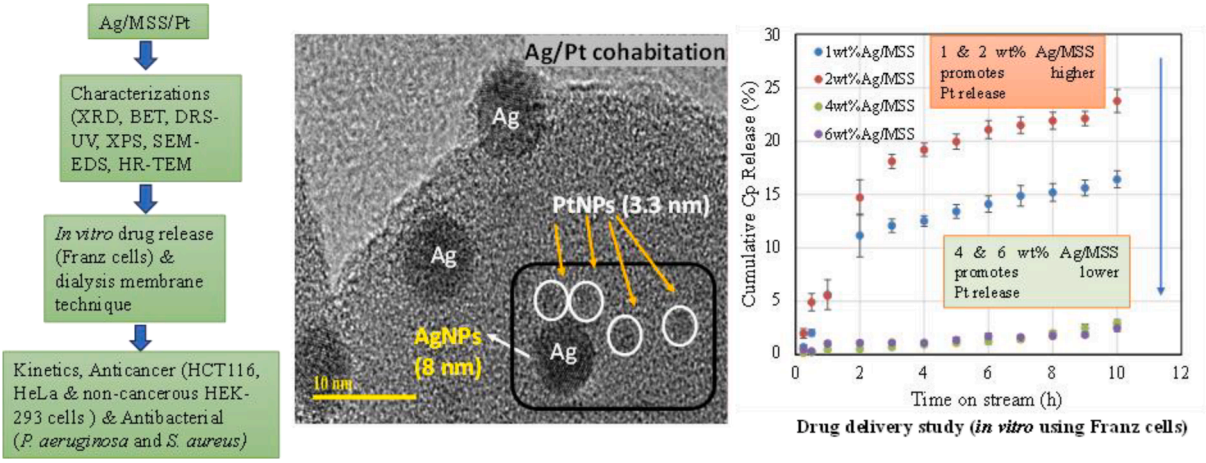

Scheme 1. Controlling the cisplatin release by synergistic action of silver and cisplatin for targeted cancer therapy.

Deanship of Scientific Research (DSR), Imam Abdulrahman Bin Faisal University with grant number 2020–165-IRMC.

CRediT authorship contribution statement

Suriya Rehman: Methodology, Investigation, Writing – original draft. **Vijaya Ravinayagam:** Conceptualization, Writing – review & editing. **Suhailah S. Al-Jameel:** Methodology, Formal analysis, Investigation. **Syed Mehmood Ali:** Methodology, Data curation, Investigation. **Sukainah Z. Alzayer:** Investigation, Formal analysis. **Zahrah M. Alfaraj:** Methodology, Formal analysis, Investigation. **Atheer Alboeid:** Methodology, Data curation, Investigation. **Nawal Alamri:** Methodology, Formal analysis. **Sakinah H Al Isam:** Investigation, Data curation, Writing – original draft. **H. Dafallae:** Visualization, Writing – review & editing. **Sugapriya Dhanasekaran:** Visualization, Writing – review & editing. **Gazali Tanimu:** Investigation, Methodology. **Firdos Alam Khan:** Methodology, Investigation, Writing – original draft. **B. Rabindran Jermy:** Conceptualization, Investigation, Methodology, Writing – original draft.

Declaration of competing interest

The authors declare that they have no known competing financial interests or personal relationships that could have appeared to influence the work reported in this paper.

Acknowledgments

The authors would like to acknowledge the advanced state of art facilities provided by Institute for Research and Medical Consultations (IRMC), Imam Abdulrahman Bin Faisal University, Dammam, Saudi Arabia. The author would like to thank Prof. Munirah Almessiere for XPS analysis.

Appendix A. Supplementary material

Supplementary data to this article can be found online at https://doi.org/10.1016/j.arabjc.2024.105661.

References

Abdulrehman, T., Qadri, S., Skariah, S., Sultan, A., Mansour, S., Azzi, J., et al., 2020. Boron doped silver-copper alloy nanoparticle targeting intracellular S. aureus in bone cells. PLoS One 15 (4), e0231276.

Ahmadian, E., Dizaj, S.M., Rahimpour, E., Hasanzadeh, A., Eftekhari, A., Hosain Zadegan, H., Halajzadeh, J., Ahmadian, H., 2018. Effect of silver nanoparticles in the induction of apoptosis on human hepatocellular carcinoma (HepG2) cell line. Mater Sci Eng C Mater Biol Appl. 93, 465–471. https://doi.org/10.1016/j.msec.2018.08.027.

Alavi, M., Rai, M., Martinez, F., Kahrizi, D., Khan, H., Rose Alencar De Menezes, I., Douglas Melo Coutinho, H., Costa, J.G.M., 2022. The efficiency of metal, metal oxide, and metalloid nanoparticles against cancer cells and bacterial pathogens: different mechanisms of action. Cell. Mol. Biomed. Rep. 2(1), 10-21. doi: 10.55705/CMBR.2022.147090.1023.

Aldossary, H.A., Rehman, S., Jermy, B.R., AlJindan, R., Aldayel, A., AbdulAzeez, S., Akhtar, S., Khan, F.A., Borgio, J.F., Al-Suhaimi, E.A., 2022. Therapeutic Intervention for Various Hospital Setting Strains of Biofilm Forming Candida auris with Multiple Drug Resistance Mutations Using Nanomaterial Ag-Silicalite-1 Zeolite. Pharmaceutics 14, 2251. https://doi.org/10.3390/pharmaceutics14102251.

Al-Enazi, N.M., Alsamhary, K., Kha, M., Ameen, F., 2023. In vitro anticancer and antibacterial performance of biosynthesized Ag and Ce co-doped ZnO NPs. Bioprocess Biosyst. Eng. 46 (1), 89–103. https://doi.org/10.1007/s00449-022-02815-8.

Alomari, M., Jermy, B.R., Ravinayagam, V., Akhtar, S., Almofty, S.A., Rehman, S., Bahmdan, H., AbdulAzeez, S., Borgio, J.F., 2019. Cisplatin-functionalized three-dimensional magnetic SBA-16 for treating breast cancer cells (MCF-7). Artif. Cells Nanomed. Biotechnol. 47 (1), 3079–3086. https://doi.org/10.1080/21691401.2019.1645155.

Baig, U., Gondal, M.A., Rehman, S., Akhtar, S., 2020. Facile Synthesis; Characterization of Nano-Tungsten Trioxide Decorated with Silver Nanoparticles and Their Antibacterial Activity against Water-Borne Gram-Negative Pathogens. Applied Nanoscience (switzerland) 10, 851–860. https://doi.org/10.1007/s13204-019-01186-z.

Balasamy, R.J., Ravinayagam, V., Alomari, M., Ansari, M.A., Almofty, S.A., Rehman, S., Dafalla, H., Marimuthu, P.R., Akhtar, S., Al Hamad, M., 2019. Cisplatin delivery, anticancer and antibacterial properties of Fe/SBA-16/ZIF-8 nanocomposite. RSC Adv. 9 (72), 42395–42408. https://doi.org/10.1039/C9RA07461A.

Chandrakala, V., Aruna, V., Angajala, G., 2022. Review on metal nanoparticles as nanocarriers: Current challenges and perspectives in drug delivery systems. Emergent Materials 5, 1593–1615. https://doi.org/10.1007/s42247-021-00335-x.

Chang, S., Bao, H., Huang, W., 2022. Size-Dependent Redispersion or Agglomeration of Ag Clusters on CeO2. J. Phys. Chem. C 126 (28), 11537–11543. https://doi.org/10.1021/acs.jpcc.2c01207.

Chen, L., Ma, D., Zhang, Z., Guo, Y., Ye, D., Huang, B., 2012. Synergistic Effect of a Carbon Black Supported PtAg Non-Alloy Bimetal Nanocatalyst for CO Preferential Oxidation in Excess Hydrogen. ChemCatChem 4 (12), 1960–1967. https://doi.org/10.1002/cctc.201200365.

Dalby, K.N., Nesbitt, H.W., Zakaznova-Herzog, V.P., King, P.L., 2007. Resolution of bridging oxygen signals from O 1s spectra of silicate glasses using XPS: Implications for O and Si speciation. Geochim. Cosmochim. Acta 71 (17), 4297–4313. https://doi.org/10.1016/j.gca.2007.07.005.

Dubey, P., Sertorio, M., Takiar, V., 2022. Therapeutic advancements in metal and metal oxide nanoparticle-based radiosensitization for head and neck cancer therapy. Cancers 14 (3), 514. https://doi.org/10.3390/cancers14030514.

Elsayed, K.A., Alomari, M., Drmosh, Q.A., Alheshibri, M., Al Baroot, A., Kayed, T.S., Manda, A.A., Al-Alotaibi, A.L., 2022. Fabrication of ZnO-Ag bimetallic nanoparticles by laser ablation for anticancer activity. Alex. Eng. J. 61 (2), 1449–1457. https://doi.org/10.1016/j.aej.2021.06.051.

Firet, N.J., Blommaert, M.A., Burdyny, T., Venugopal, A., Bohra, D., Longo, A., Smith, W. A., 2019. Operando EXAFS study reveals presence of oxygen in oxide-derived silver catalysts for electrochemical CO 2 reduction. J. Mater. Chem. A 7 (6), 2597–2607. https://doi.org/10.1039/C8TA10412C.

Gao, P., Chang, X., Zhang, D., Cai, Y., Chen, G., Wang, H., Wang, T., 2021. Synergistic integration of metal nanoclusters and biomolecules as hybrid systems for therapeutic applications. Acta Pharm. Sin. B 11 (5), 1175–1199. https://doi.org/10.1016/j.apsb.2020.12.004.

Gharibshahi, E., Saion, E., 2012. Influence of dose on particle size and optical properties of colloidal platinum nanoparticles. Int. J. Mol. Sci. 13 (11), 14723–14741. https://doi.org/10.3390/ijms131114723.

Gilani, S.J., Bin-Jumah, M.N., Al-Abbasi, F.A., Nadeem, M.S., Alzarea, S.I., Ahmed, M.M., Sayyed, N., Kazmi, I., 2022. Rosinidin Protects against Cisplatin-Induced Nephrotoxicity via Subsiding Proinflammatory and Oxidative Stress Biomarkers in Rats. Int. J. Environ. Res. Public Health 19 (15), 9719. https://doi.org/10.3390/ijerph19159719.

Hashem, A.H., El-Sayyad, G.S., 2023. Antimicrobial and anticancer activities of biosynthesized bimetallic silver-zinc oxide nanoparticles (Ag-ZnO NPs) using pomegranate peel extract. Biomass Convers. Biorefin. 1–13 https://doi.org/10.1007/s13399-023-04126-8.

Helmiyati Novientri, G., Abbas, G.H., Budianto, E., 2019. Nanocomposite Hydrogel-Based Biopolymer Modified with Silver Nanoparticles as an Antibacterial Material for Wound Treatment. Journal of Applied Pharmaceutical Science 9 (11), 001–009. https://doi.org/10.7324/JAPS.2019.91101.

Hemlata, Meena, P.R., Singh, A.P., Tejavath, K.K., 2020. Biosynthesis of silver nanoparticles using Cucumis prophetarum aqueous leaf extract and their antibacterial and antiproliferative activity against cancer cell lines. ACS omega, 5 (10), 5520–5528. doi.org/10.1021/acsomega.0c00155.

Jermy, B.R., Acharya, S., Ravinayagam, V., Alghamdi, H.S., Akhtar, S., Basuwaidan, R.S., 2018. Hierarchical mesosilicalite nanoformulation integrated with cisplatin exhibits target-specific efficient anticancer activity. Appl. Nanosci. 8 (5), 1205–1220.

Jermy, R., Ravinayagam, V., Alamoudi, W., Almohazey, D., Elanthikkal, S., Dafalla, H., Rehman, S., Chandrasekar, G., Baykal, A., 2020. Tuning pH sensitive chitosan and cisplatin over spinel ferrite/silica nanocomposite for anticancer activity in MCF-7 cell line. J. Drug Delivery Sci. Technol. 57, 101711 https://doi.org/10.1016/j.jddst.2020.101711.

Kasinathan, K., Marimuthu, K., Murugesan, B., Samayanan, S., Panchu, S.J., Swart, H.C., Savariroyan, S.R.I., 2021. Synthesis of biocompatible chitosan functionalized Ag decorated biocomposite for effective antibacterial and anticancer activity. Int. J. Biol. Macromol. 178, 270–282. https://doi.org/10.1016/j.ijbiomac.2021.02.127.

Khan, F.A., Akhtar, S., Almohazey, D., Alomari, M., Almofty, S.A., Eliassari, A., 2018. Fluorescent Magnetic Submicronic Polymer (FMSP) Nanoparticles Induce Cell Death in Human Colorectal Carcinoma Cells. Artificial Cells; Nanomedicine and Biotechnology. 46 (sup3) https://doi.org/10.1080/21691401.2018.1491476.

Kovács, D., Igaz, N., Gopisetty, M.K., Kiricsi, M., 2022. Cancer therapy by silver nanoparticles: fiction or reality? Int. J. Mol. Sci. 23 (2), 839. https://doi.org/10.3390/ijms23020839.

Kumar, S., Shukla, M.K., Sharma, A.K., Jayaprakash, G.K., Tonk, R.K., Chellappan, D.K., Singh, S.K., Dua, K., Ahmed, F., Bhattacharyya, S., Kumar, D., 2023. Metal-based nanomaterials and nanocomposites as promising frontier in cancer chemotherapy. MedComm 4 (2), e253.

Lara, H.H., Ayala-Núñez, N.V., Ixtepan Turrent, L.D.C., Rodríguez Padilla, C., 2010. Bactericidal effect of silver nanoparticles against multidrug-resistant bacteria. World J. Microbiol. Biotechnol. 26, 615–621. https://doi.org/10.1007/s11274-009-0211-3.

Li, L., Wang, X., Shen, J., Zhou, L., Zhang, T., 2005. Study on chemisorption of H2, O2, CO and C2H4on Pt-Ag/SiO2catalysts by microcalorimetry and FTIR. J. Therm. Anal. Calorim. 82 (1), 103–107. https://doi.org/10.1007/s10973-005-0848-6.

Lin, W., Huang, Y.W., Zhou, X.D., Ma, Y., 2006. In vitro toxicity of silica nanoparticles in human lung cancer cells. Toxicol. Appl. Pharmacol. 217 (3), 252–259. https://doi.org/10.1016/j.taap.2006.10.004.

Mateo, E.M., Jiménez, M., 2022. Silver Nanoparticle-Based Therapy: Can It Be Useful to Combat Multi-Drug Resistant Bacteria? Antibiotics 11, 1205. https://doi.org/10.3390/antibiotics11091205.

Meister, T.L., Fortmann, J., Breisch, M., Sengstock, C., Steinmann, E., Köller, M., Pfaender, S., Ludwig, A., 2022. Nanoscale copper and silver thin film systems display differences in antiviral and antibacterial properties. Sci. Rep. 12 (1), 7193. https://doi.org/10.1038/s41598-022-11212-w.

Mohanbaba, S., Gurunathan, S., 2016. Differential Biological Activities of Silver Nanoparticles against Gramnegative and Gram-Positive Bacteria: A Novel Approach for Antimicrobial Therapy. Nanobiomaterials in Antimicrobial Therapy: Applications of Nanobiomaterials 6, 193–227. https://doi.org/10.1016/B978-0-323-42864-4.00006-3.

Mosselhy, D.A., Granbohm, H., Hynönen, U., Ge, Y., Palva, A., Nordström, K., Hannula, S.-P., 2017. Nanosilver-Silica Composite: Prolonged Antibacterial Effects and Bacterial Interaction Mechanisms for Wound Dressings. Nanomaterials 7, 261. https://doi.org/10.3390/nano7090261.

Ni, C., Zhong, Y., Wu, W., Song, Y., Makvandi, P., Yu, C., Song, H., 2022. Co-delivery of nano-silver and vancomycin via silica nanopollens for enhanced antibacterial functions. Antibiotics 11 (5), 685. https://doi.org/10.3390/antibiotics11050685.

Niculescu, V.C., 2020. Mesoporous silica nanoparticles for bio-applications. Front. Mater. 7, 36. https://doi.org/10.3389/fmats.2020.00036.

Niu, Y., Tang, E., Zhang, Q., 2019. Cytotoxic effect of silica nanoparticles against hepatocellular carcinoma cells through necroptosis induction. Toxicol. Res. 8 (6), 1042–1049. https://doi.org/10.1039/c9tx00240e.

Oh, H.S., Yang, J.H., Costello, C.K., Wang, Y.M., Bare, S.R., Kung, H.H., Kung, M.C., 2002. Selective Catalytic Oxidation of CO: Effect of Chloride on Supported Au Catalysts. J. Catal. 210, 375–386. https://doi.org/10.1006/jcat.2002.3710.

Rehman, S., Jermy, R., Asiri, S.M., Shah, M.A., Farooq, R., Ravinayagam, V., Ansari, M. A., Alsalem, Z., Al Jindan, R., Reshi, Z., Khan, F.A., 2020a. Using Fomitopsis pinicola for bioinspired synthesis of titanium dioxide and silver nanoparticles, targeting biomedical applications. RSC Adv. 10 (53), 32137–32147. https://doi.org/10.1039/D0RA02637A.

Rehman, S., Asiri, S.M., Khan, F.A., Jermy, B.R., Ravinayagam, V., Alsalem, Z., Jindan, R. A., Qurashi, A., 2020b. Anticandidal and in vitro anti-proliferative activity of sonochemically synthesized indium tin oxide nanoparticles. Sci. Rep. 10 (1), 1–9. https://doi.org/10.1038/s41598-020-60295-w.

Roy, A., Mukhopadhyay, A.K., Das, S.C., Bhattacharjee, G., Majumdar, A., Hippler, R., 2019. Surface Stoichiometry and Optical Properties of Cu x–Ti y C z Thin Films Deposited by Magnetron Sputtering. Coatings 9 (9), 551. https://doi.org/10.3390/coatings9090551.

Santos, H.S., Sliz, R., Nguyen, H., Srivastava, S., Ramteke, D., Fabritius, T., Lassi, U., Kinnunen, P., 2022. Hybrid amorphous-crystalline silicate composites as feasible solid-state electrolytes. Mater. Des. 217, 110599 https://doi.org/10.1016/j.matdes.2022.110599.

Senapati, S., Mahanta, A.K., Kumar, S., Maiti, P., 2018. Controlled drug delivery vehicles for cancer treatment and their performance. Signal Transduct. Target. Ther. 3 (1), 7. https://doi.org/10.1038/s41392-017-0004-3.

Shu, Z., Zhang, Y., Yang, Q., Yang, H., 2017. Halloysite nanotubes supported Ag and ZnO nanoparticles with synergistically enhanced antibacterial activity. Nanoscale Res. Lett. 12 (1), 1–7. https://doi.org/10.1186/s1167-017-1859-5.

Singh, C., Mehata, A.K., Priya, V., Malik, A.K., Setia, A., Suseela, M.N.L., Vikas, G., Samridhi, P., Singh, S.K., Muthu, M.S., 2022. Bimetallic Au–Ag nanoparticles: advanced nanotechnology for tackling antimicrobial resistance. Molecules 27 (20), 7059. https://doi.org/10.3390/molecules27207059.

Spitzmüller, L., Nitschke, F., Rudolph, B., Berson, J., Schimmel, T., Kohl, T., 2023. Dissolution control and stability improvement of silica nanoparticles in aqueous media. J. Nanopart. Res. 25 (3), 40. https://doi.org/10.1007/s11051-023-05688-4.

Stamenkovic, V., Mun, B.S., Mayrhofer, K., Ross, P.N., Markovic, N.M., Rossmeisl, J., Greeley, J., Nørskov, J.K., 2006. Changing the Activity of Electrocatalysts for Oxygen Reduction by Tuning the Surface Electronic Structure. Angew. Chem. 118, 2963–2967. https://doi.org/10.1002/ange.200504386.

Subhan, M.A., Muzibur Rahman, M., 2022. Recent development in metallic nanoparticles for breast cancer therapy and diagnosis. Chem. Rec. 22 (7), e202100331.

Urnukhsaikhan, E., Bold, B.E., Gunbileg, A., Sukhbaatar, N., Mishig-Ochir, T., 2021. Antibacterial activity and characteristics of silver nanoparticles biosynthesized from Carduus crispus. Sci. Rep. 11 (1), 1–12. https://doi.org/10.1038/s41598-021-00520-2.

Wang, D., Zhao, P., Li, Y., 2011. General preparation for Pt-based alloy nanoporous nanoparticles as potential nanocatalysts. Sci. Rep. 1 (1), 37. https://doi.org/10.1038/srep00037.

Yan, F., Zhang, H., Zhang, Y., Yang, F., 2021. Agglomeration of Pt nanoparticles on the g-C3N4 surface dominated by oriented attachment mechanism and way of inhibition. Mater. Res. Express 8 (5), 055504. https://doi.org/10.1088/2053-1591/abfde6.

Yang, M., Lu, F., Zhou, T., Zhao, J., Ding, C., Fakhri, A., Gupta, V.K., 2020. Biosynthesis of nano bimetallic Ag/Pt alloy from Crocus sativus L. extract: Biological efficacy and catalytic activity. J. Photochem. Photobiol. B Biol. 212, 112025 https://doi.org/10.1016/j.jphotobiol.2020.112025.

Yu, W., Dong, Q., Yu, W., Wan, Q., Chen, X., 2022. Facile Preparation of MCM-41/Ag2O Nanomaterials with High Iodide-Removal Efficiency. Nanomaterials 12 (20), 3678. https://doi.org/10.3390/nano12203678.

Zhan, H., Zhou, X., Cao, Y., Jagtiani, T., Chang, T.-L., Liang, J.F., 2017. Anti-cancer activity of camptothecin nanocrystals decorated by silver nanoparticles. J. Mater. Chem. B 5 (14), 2692–2701. https://doi.org/10.1039/C7TB00134G.

Zhang, Y., Li, Y., Gao, Z., Ding, B., An, P., Zhang, X., Sun, B., Sun, B., 2020. Mesoporous silica-coated silver nanoframes as drug-delivery vehicles for chemo/starvation/metal ion multimodality therapy. Langmuir 36 (23), 6345–6351. https://doi.org/10.1021/acs.langmuir.0c00191.

Zhao, X., Qi, T., Kong, C., Hao, M., Wang, Y., Li, J., Liu, B., Gao, Y., Jiang, J., 2018. Photothermal exposure of polydopamine-coated branched Au-Ag nanoparticles induces cell cycle arrest, apoptosis, and autophagy in human bladder cancer cells. Int. J. Nanomed. 13, 6413–6428. https://doi.org/10.2147/IJN.S174349.

Zou, J., Zhu, B., Li, Y., 2020. Functionalization of Silver Nanoparticles Loaded with Paclitaxel-induced A549 Cells Apoptosis Through ROS-Mediated Signaling Pathways. Curr. Top. Med. Chem. 20 (2), 89–98. https://doi.org/10.2174/1568026619666191019102219.